JAAS

PAPER

View Article Online
View Journal | View Issue

Cite this: J. Anal. At. Spectrom., 2016, 31, 2198

Compressed sensing spectral imaging for plasma optical emission spectroscopy

John D. Usala,[a] Adrian Maag,[ab] Thomas Nelis[b] and Gerardo Gamez*[a]

Plasma optical emission spectral imaging is critical for the development of chemical analysis applications and plasma diagnostics. Nevertheless, typical techniques require array detectors that can be very expensive or pixel-to-pixel rastering approaches that are highly time-consuming. Further, the acquired image files are compressed to keep data manageable, which can be achieved without loss of critical information, thus showing the sparsity of the data. A fairly recent paradigm in sampling, compressed sensing (CS), allows performing compression during acquisition which results in a more efficient use of experimental resources. As such, CS systems can be much faster, cost-effective, or even provide better resolution or throughput. In this study, a CS spectral imaging system, featuring a single-sensor and a variable encoding mask, is designed and implemented for plasma optical emission spectroscopy. The performance, based on PSNR and spatial resolution, is characterized as a function of experimental and image processing parameters such as sensing matrix selection, recovery algorithm choice, and sparsifying basis. Spectral images of optical emissions from plasma species of interest (He I, N_2, N_2^+) were collected from an atmospheric pressure plasma jet. The use of a CS spectral imaging system for plasma diagnostics (T_{vib}) is reported for the first time.

Received 19th July 2016
Accepted 27th September 2016

DOI: 10.1039/c6ja00261g

www.rsc.org/jaas

Introduction

Spectral imaging is an important tool in the chemical analysis arsenal that allows obtaining spatially-resolved qualitative and quantitative information. Such information is important to improve the understanding of samples of interest as well as optimize the performance of relevant systems. In the case of plasma optical emission spectroscopy (OES), spectral imaging plays a critical role in application development, for example in the case of glow discharge surface elemental mapping[1,2] or inductively coupled plasma matrix-effect flagging.[3,4] In addition, spectral imaging has become essential in plasma fundamental studies for glow discharge,[5,6] inductively coupled plasma,[7–9] dielectric barrier discharges,[10,11] laser induced breakdown plasmas,[12,13] *etc.*, to better understand the underlying plasma mechanisms.

The spectral data cube information, intensity as a function of two spatial dimensions and the spectral dimension, is typically obtained with 2D array detectors by collecting the intensity simultaneously in two dimensions and scanning the remaining dimension. Such array detectors may function well for spectral imaging but they reach higher costs as more complex features (chip size, number of pixels, temporal resolution, intensifiers, *etc.*) are included. The expense can be prohibitive (several tens of thousands USD) to develop certain applications or for using spectral imaging plasma diagnostics routinely.

A more cost-effective approach would entail using a detector with a single sensor and rastering, that is, collecting the spectrally resolved intensity at adjacent positions of the object until the whole image is obtained. On the other hand, this approach is increasingly time-consuming to the point of becoming impractical, depending on the analysis time per spot and the number of spots per image. To circumvent the problem of long acquisition times with a single sensor, compressed sensing may be implemented.[14] Compressed sensing (CS) is a relatively new sampling paradigm that allows one to under-sample with respect to the Nyquist criteria (sampling rate >2× the frequency of the signal of interest) and still obtain an image of comparable fidelity.[15–22] For example, if one desires to obtain a 10 × 10 pixel map, under traditional imaging, 100 individual measurements would be required: one measurement per pixel. On the other hand, compressed sensing allows obtaining an image of comparable resolution with significantly less measurements.

Several excellent materials are available to get a better understanding of compressed sensing.[15–22] In fact, a tutorial review of CS in analytical spectroscopy is concurrently published in this issue.[23] Nevertheless, the following case will serve to gain a better understanding of the basic compressed sensing approach here. In traditional imaging an image such as a resolution target or the emission from a plasma is projected onto a camera, which is a 2D array of N pixels. This projection

[a]Texas Tech University, Department of Chemistry and Biochemistry, Lubbock, TX 79409-41061, USA. E-mail: gerardo.gamez@ttu.edu

[b]Berner Fachhochschule Technik und Informatik, Institute ALPS, Quellgasse 21, CH-2501 Biel-Bienne, Switzerland

corresponds to a matrix of N measurements. In the CS approach implemented here, instead of a 2D array detector the image is projected onto a spatial light modulator (SLM) that acts as a mask to allow selected sections of the image (*i.e.* an encoded image) to simultaneously reach a single pixel detector. In this fashion, a series of randomly generated masks result in the single pixel measuring a series of encoded light intensity signals. The random nature of the mask generation ensures an equal probability of all of the sections of the image to be measured. This process can be mathematically represented as follows: each mask pattern projected by the SLM is a matrix that can be concatenated and transposed to become a row of a larger sensing matrix, A, which includes all the projected mask patterns as rows. The sensing matrix, A, is applied to the sample matrix, x, which is the concatenated version of the sample image matrix to be measured:

$$Ax = y$$

The result is the measurement vector, y, in which each element is the encoded intensity measured at the single pixel detector for each corresponding randomly generated mask. In traditional imaging, the sensing matrix A would look like a square matrix because there would be an equal number of measurements (rows) *vs.* the number of pixels (columns). In this sense, the system is determined, same number of equations as unknowns, and has a unique solution. In compressive sensing, A is a rectangular "fat" matrix because there are fewer measurements than pixel values and the system is underdetermined.

Although there are infinitely many solutions to an underdetermined system of equations, CS recovers signals in fewer measurements than traditional means by two principles: sparsity and incoherence.[22] A signal is sparse when most of its information is contained in a few elements, for example, a spectrum with only a couple of sharp peaks. However, even when at first glance a signal does not seem sparse, or compressible, it may be sparse when it is represented in a different basis (or domain), for example, a complex waveform in the time domain may be represented by only a few peaks in the frequency domain through a Fourier transform. The change of basis does not change the intrinsic information contained in the signal but rather the way it is represented so that the majority of the signal is contained in fewer elements. Sparsity is a property traditionally exploited in software file compression after signal acquisition. In contrast, compressive sensing features compression during the signal acquisition by taking advantage of the sparsity of the signal.

Next, a suitable measurement matrix that is incoherent with respect to the sparsifying basis must be used. Coherence, in this case, is a measure of the correlation between the sensing matrix and the signal basis representation. In compressive sensing, incoherent systems yield the most efficient sampling, *i.e.* require the least number of samples for signal reconstruction. Ideally, the measurement matrix would consist of completely independent and identically distributed entries to ensure minimum coherence. In the CS imaging system implemented here, this translates into random generation of the masks applied to the SLM, *i.e.* randomly selecting which parts of the image reach the detector, through the use of structurally random matrices. A high degree of randomness is key to an efficient sensing matrix design, although this is not always feasible in physical implementations.

Finally, compressive sensing reconstructs the system of underdetermined equations using various minimization algorithms.[24] The techniques are all problems in convex minimization. Such algorithms include interior-point, matching pursuit, and gradient projection methods. All reconstruction algorithms strive to find the sparsest solution to the original linear programmable problem.

Baraniuk *et al.*[14] took advantage of compressed sensing principles to develop a single-pixel camera, featuring a photodiode for IR imaging. The setup includes a digital micromirror device to generate a series of pseudo-random binary masks to encode the light from the object that arrives at the detector. The under-sampled measurements are then used to reconstruct the image through compressed sensing algorithms. This approach allowed a much more cost effective solution to array detectors.

In this work a monochromator with a photomultiplier tube and a digital micromirror device (DMD) are used to develop a single detector compressed sensing spectral imager. A sensing matrix, A, design called the scrambled block Hadamard ensemble[25] is used to allow for fast reconstruction and adaptability to different levels of light. The system is characterized in terms of fidelity and resolution by comparing the performance with two different sparsifying basis and two reconstruction algorithms. The instrument capabilities are demonstrated by obtaining spectral images of an atmospheric pressure plasma jet.

Experimental methods

CS spectral imaging system

The light emitted from the object was collected through a collimating lens and focused with a second lens onto a DMD (DLP® LightCrafter™ Evaluation Module with DLP 0.3 WVGA chipset, Texas Instruments) (Fig. 1a). An area of 512 × 512 mirrors was used with 2 × 2 binning giving 256 × 256 pixel images. The mirrors of the DMD are aligned in a diamond grid such that the lines in one dimension are straight and in the other they are zigzag which results in the interline distance being twice in one dimension *vs.* the other. Thus, the height of each resultant image had to be adjusted by a factor of $\frac{1}{2}$. The multiplexed light was then collected through another series of collimating and focusing lenses and was focused onto the entrance slit of a monochromator (Bentham M300, 1200 g mm^{-1}). The bandpass of the monochromator for plasma images was 1.76 nm. All lenses had the following characteristics: UV fused silica plano-convex, uncoated, $f = 200.7$ mm, Ø2. The monochromator was equipped with a PMT (R6358P, Hamamatsu). An in-house built preamplifier, amplifier, and offset modulator were used to condition the signal. The signal was then recorded through an analogue-to-digital converter (USB-6001 14-Bit, National Instruments) at 2.5 kHz.

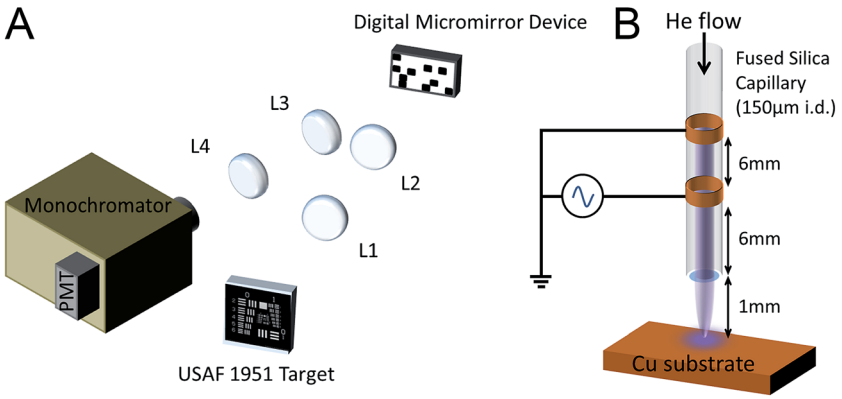

Fig. 1 (A) Diagram of the compressed sensing spectral imaging system. L1 and L2 transfer the light onto a DMD for encoding with a series of patterns. The light is then sent through a monochromator equipped with a PMT for detection. (B) Diagram of the APPJ used for CS spectral imaging of plasma optical emission spectroscopy. See text for operating conditions.

Measurements were taken and reconstructions were performed with a Windows operating system laptop with an Intel® Core™ i7-5600U CPU @ 2.60 GHz and 16 GB RAM.

Plasma source

The atmospheric pressure plasma jet consisted of a dielectric barrier discharge (DBD) operated with He gas (Fig. 1b). The DBD jet was produced by placing two aluminum foil electrodes wrapped outside with a silica capillary (150 μm id., 300 μm od.) at a distance of 6 mm from each other. One electrode was grounded and the other connected to an AC power supply (PVM500, Information Unlimited) operated at 30 kHz and an applied voltage of 8 kV. The powered electrode was placed 6 mm from the capillary end. The He gas flow was maintained at 0.4 slpm. A copper block placed 1 mm from the capillary end was used as a model sample.

Software

Sensing and reconstruction design was performed with the Structurally Random Matrix toolbox Version 1.0. The fast_csd.m example was adapted for measurements using the DMD. Scrambled Block Hadamard Ensemble (SBHE) structurally random matrices (SRMs) were used as the sensing matrix, written into video files and streamed *via* HDMI to the DMD. As

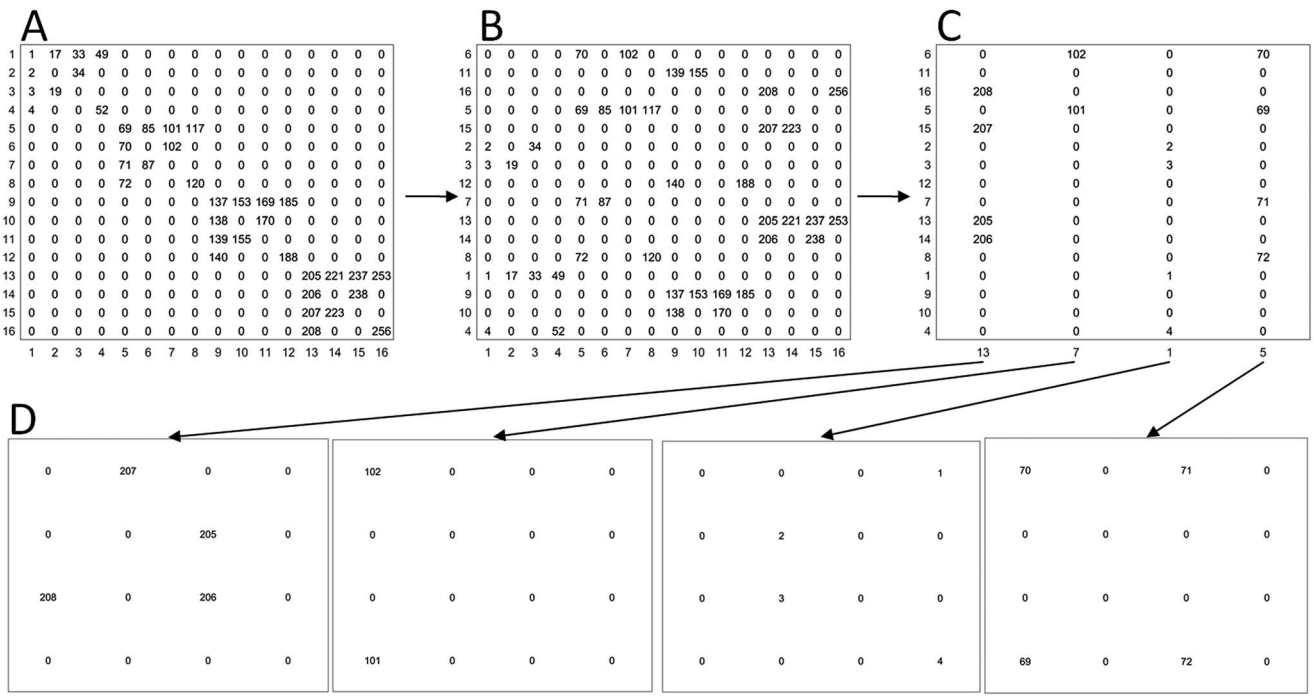

Fig. 2 Flow diagram of the sequence for constructing the scrambled block Hadamard matrices. (A) Matrix diagonally blocked with Hadamard matrix. (B) Rows randomized. (C) Randomly selected columns. (D) Columns reshaped into matrices for a 4 × 4 coded mask sequence example. The specific numbers inside the matrices are only there to facilitate following the example flow. In practice, each number would correspond to an ON mirror on the DMD which directs light toward the detector.

opposed to stored random matrices, SRMs have the advantage of fast computation during reconstruction. Fig. 2 depicts an example of the SBHE generation process with a 4 × 4 Hadamard block to create the patterns for a 4 × 4 DMD section. The SBHE is created by diagonally arranging blocks of the Hadamard matrix with the selected size, in this case 4 × 4, onto a larger matrix (Fig. 2a). If the Hadamard is composed of 1's and −1's, then the −1's are changed to zero. Next, the rows of the matrix are randomized (Fig. 2b). Subsequently, a subset of columns is selected at random (Fig. 2c). It is important to note that the act of randomizing the rows and selecting the columns at random must be seeded to be able to account for it during the reconstruction process. Each resultant column is reshaped to a matrix and sequentially applied as a pattern on the DMD (Fig. 2d). The Hadamard blocks implemented for the matrices used in the measurements here had sizes of 512 × 512, 1024 × 1024, 2046 × 2046, and 4096 × 4096.

Patterns were written into a video file by repeating a pattern with two frames and then inserting an off frame between patterns. Pattern repetition was implemented to account for error in the display time of the DMD, and off frames were used to better differentiate between the resultant signals. Finally, the script was run at 30 frames per second. Thus, three frames were used per pattern, (2 repeated and 1 off) and the pattern rate was 10 patterns per second.

The reconstruction algorithms used included Gradient Projection for Sparse Reconstruction (GPSR),[26] a gradient projection type solver that has a penalty term derived from a scaled l1-norm and a least-squares term, and Two-step Iterative Shrinking/Thresholding Algorithm for Linear Inverse Problems (TwIST),[27] a second order two-step iterative shrinkage algorithm. These were selected because they are known to be faster compared to others.[24] With respect to sparsifying basis, both the Discrete Cosine Transform (DCT) and the 9–7 Discrete Wavelet Transform (DWT) were used.

Results and discussion

The system characterization and optimization was performed by imaging a USAF 1951 Airforce target back illuminated with a desk lamp. Fig. 3 shows sample images obtained at selected conditions. It is evident by simple eye inspection that there are differences among the images but a quantitative comparison was undertaken by calculating the compression fidelity.

Compression fidelity

The compression fidelity of the system was quantified by calculating the Peak Signal-to-Noise Ratio (PSNR). The PSNR is defined by:

$$\mathrm{PSNR} = 10 \log_{10}\left(\frac{\mathrm{MAX}_I{}^2}{\mathrm{MSE}}\right)$$

$$\mathrm{MSE} = \frac{1}{mn}\sum_{i=0}^{m-1}\sum_{j=0}^{n-1}\left[I(i,j) - K(i,j)\right]^2$$

The mean squared error (MSE) is used to perform a pixel-to-pixel comparison between a standard image I, made up of $m \times n$ pixels, and the reconstructed same-size image resulting from compressed sampling, K. The PSNR is obtained by weighing the

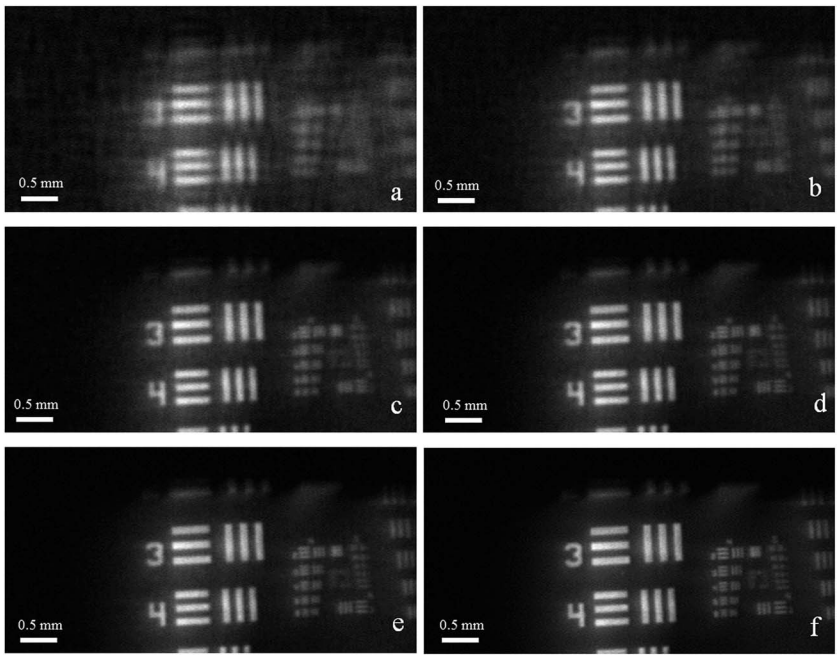

Fig. 3 Images of USAF 1951 target acquired with 512 block size SBHE and reconstructed with GPSR algorithm with DCT. The effect of compression can be observed at percent samplings of 10% (a), 20% (b), 30% (c), 40% (d), 50% (e), and 100% (f), *i.e.* the number of measurements with respect to the total number of pixels.

MSE *vs.* the maximum possible value (MAX) according to the bit depth (8 bit in our case) and expressed in decibels to better manage high dynamic ranges. Higher PSNR is interpreted as better compression fidelity. An ideal standard image would be obtained by rastering pixel-by-pixel to represent the traditional sampling approach. Nevertheless, that type of standard image could not be obtained because the signal-to-noise ratio was limiting and increasing acquisition times was impractical. Thus, the standard image was sampled in a similar fashion as the compressed sensing images using a 512 SBHE but letting the number of samples, or measurements, equal the number of pixels, *i.e.* no compression. For the standard image, the resulting determined system of equations was solved *via* Gaussian elimination, not compressed sensing algorithms, after sampling the target with an invertible matrix. Further, after the standard image was acquired, a median filter with a 2×2 neighborhood was used on the resultant image. The same median filter was applied to the images acquired *via* compressive sensing to take it into account for the PSNR calculation. Nevertheless, the challenges encountered when obtaining the standard image point to an important advantage of compressed sampling through multiplexed measurements. Also, it is worth noting that the PSNR absolute values are for comparisons with respect to another multiplexed image and not a typical sampling approach. Even so, the PSNR trends with respect to the operating and reconstruction conditions serve perfectly well for optimization. Thus, the PSNR were calculated as a function of reconstruction algorithm choice (GPSR or TwIST), basis choice (DCT or DWT), sampling percentage or compression factor, and matrix density (block Hadamard size). Finally, images were acquired with a 10% neutral density filter in order to determine the effect of light intensity.

Reconstruction algorithm and basis optimization

In order to determine the optimal basis and reconstruction algorithm choice for standard light conditions with the desk lamp, the image was sampled at a 10, 20, 30, 40, and 50% compression factor (the number of measurements divided by the total number of pixels, also known as sampling percentage) with a 512, 1024, 2048, and 4096 SBHE, totaling twenty measurements. Each image at each percent sampling and block size was reconstructed with each basis and each reconstruction algorithm. Thus a measurement at a specific percent sampling and a specific block size was reconstructed in four: GPSR with DCT, GPSR with DWT, TwIST with DCT, and TwIST with DWT.

The optimal basis was determined by performing a paired *t*-test with each reconstruction algorithm for the set of twenty measurements. Thus the difference of PSNR was measured for the GPSR–DCT and GPSR–DWT combination and the TwIST–DCT and TwIST–DWT combination. The mean difference of the GPSR basis combination was DWT > DCT by 1.98 PSNR with a *p*-value of 1.26×10^{-5}. For the TwIST algorithm combination, the mean difference was DWT > DCT by 1.72 PSNR with a *p*-value of 6.4×10^{-4}. Thus the DWT yielded a higher PSNR value with statistical significance for each of the reconstruction algorithms.

Next, the optimization of the reconstruction algorithm was determined by performing a paired *t*-test on the twenty measurements reconstructed using both TwIST and GPSR with the wavelet basis. The mean difference of reconstructions was GPSR > TwIST by 2.42 PSNR with a *p*-value of 0.0020. Thus GPSR yielded a higher PSNR value than TwIST with statistical significance for the wavelet basis. As the wavelet basis yielded a higher PSNR value than the cosine basis, the optimal reconstruction algorithm-basis combination was determined to be GPSR–DWT.

Sampling percentage and block Hadamard size

It is evident from Fig. 4 that the PSNR increases steadily from 10% sampling to 30% sampling. On the other hand, increasing the sampling percentage above 30% does not yield such significant improvements. A similar conclusion can be reached by observing the contrast measured from the intensity profile across USAF 1951 target group 4 element 1 (16 line pairs per mm) for the different sampling percentages (Fig. 5). Thus, 30% sampling was selected to measure the plasma images below in order to have high quality images at fast acquisition times.

Also evident from Fig. 4 is that smaller block sizes resulted in higher PSNR for every sampling percentage. Thus, the highest compression fidelity was attained by the 512 block size. The compressed sensing imaging process was simulated on software to better understand the PSNR trends. For this purpose, the SBHE mask matrix/pattern sequence was applied to the standard image file. The intensity of each resulting encoded image was integrated to yield a sequence of intensity values analogous to the signal measured with the CS imaging system. Subsequent reconstruction of the original image was performed as described in the experimental section. Fig. 6a shows that each of the four sizes of SBHE lead to similar PSNR values. Nevertheless, that represents an ideal case with no noise. Thus, standard white Gaussian noise was added to the simulated measurements to observe its effects. The signal-to-noise per sample, measured in dbW, was 30. The same smoothing algorithm, square pulse detection, and reconstruction algorithm

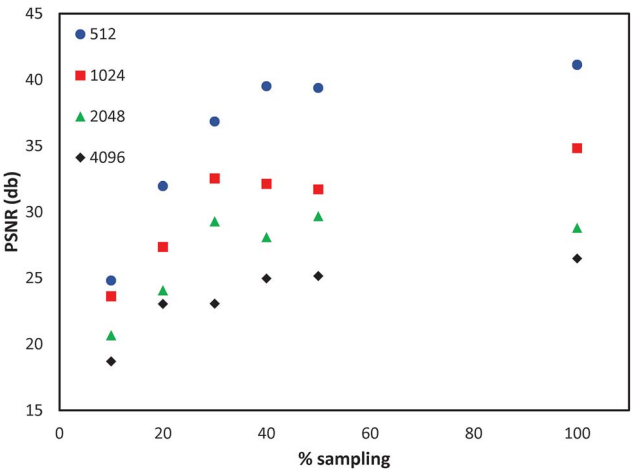

Fig. 4 PSNR as a function of percent sampling for different SBHE block sizes for images reconstructed with GPSR and DWT.

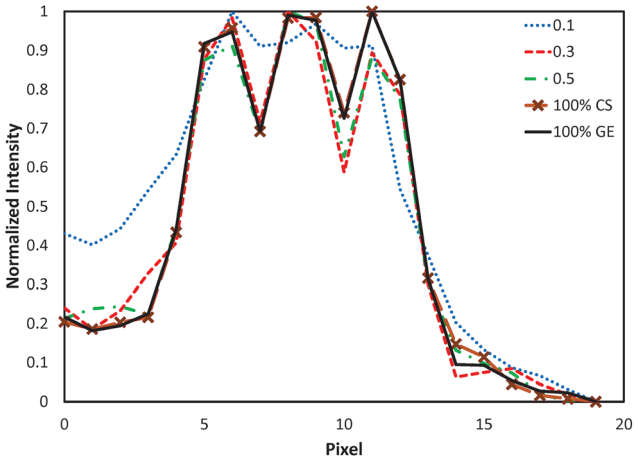

Fig. 5 Vertical intensity profile across USAF 1951 target group 4 element 1 (16 line pairs per mm) in the reconstructed images with different sampling percentages.

was then used. The resultant PSNR values in Fig. 6b show a similar trend to Fig. 4 regarding higher PSNR values for smaller block sizes.

A closer look at the signal variation within the sequence of intensity values obtained from the sequence of applied mask patterns yields an insight into the causes for the observed PSNR trends. The relative standard deviation within the sequence for the 512 SBHE is 7.39%, 1024 SBHE is 5.22%, 2048 SBHE is 3.81%, and 4096 SBHE is 2.86%. Thus, the smaller the block size, the greater the relative variation between measurements. As the noise simulation results in the same SNR irrespective of block size, the additive noise will have a greater effect on the relative variation of the signals when the block size is large. Further, the strong correlation between the simulated and experimental trend is an indication that the SNR of the experimental measurements is proportional across all block sizes. The physical source of the noise may be due to photon noise. In this case, a larger number of mirrors of the DMD that direct light toward the detector (*i.e.* larger SBHE block sizes) would result in more signal, but also in more noise. Willett and co-workers[28] have reported the effects of Poisson noise on compressed sensing imaging and found that for an image with fixed intensity the error bound increases together with the quantity of sensors.

Light intensity

Resolution target images were taken with a 10% neutral density filter in order to characterize the system's dynamic range and response to low levels of light in terms of PSNR (Fig. 7). Two noticeable differences from images taken with higher light intensity are apparent: first, low light levels resulted in overall lower PSNR values for all block sizes; second, the previously observed trend of higher PSNR with smaller block size is not present. In this case, the PSNR values were lowest for the 4096 block and increased for the 2048 block. In general, the PSNR values at 1024 were higher or similar compared to 2048. Finally, the PSNR values at 512 were lower or similar to those at 2048. A

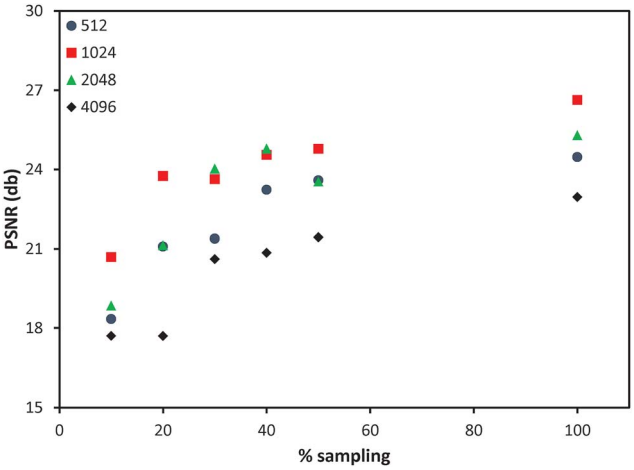

Fig. 7 PSNR as a function of percent sampling for different SBHE block sizes (GPSR, DWT) when the light intensity is decreased by an order of magnitude.

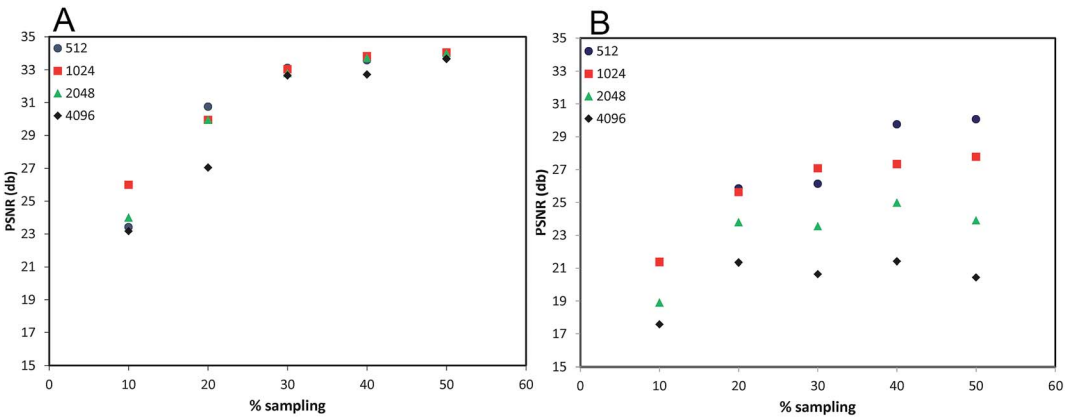

Fig. 6 PSNR as a function of percent sampling for different SBHE block sizes for simulated compressed sampling images (GPSR, DWT) without (A) and with (B) Gaussian noise added. Similar to the experimental observations, there is a trend of increasing PSNR with decreasing SBHE block size but only in the presence of noise.

plausible explanation for the different trends in block size and PSNR is the effect of signal independent noise at low light level becoming significant. Thus, at larger block sizes there are photon-noise limitations but at smaller block sizes there are signal-independent noise limitations.

With respect to other performance characteristics, it is worth noting that the acquisition time is currently limited by the DMD mirror switching frequency. Nevertheless, there are several much better DMD models in this respect that are commercially available and would allow even faster acquisition times. Furthermore, there are some wavelength range restrictions of DMDs toward the UV range with UV optimized models with recommended use only down to 360 nm.

Compressed sensing plasma optical emission spectral imaging

The newly developed CS spectral imaging system was implemented for measuring the optical emission from a dielectric barrier discharge (DBD)-based atmospheric pressure plasma jet (APPJ). APPJs have received considerable attention as ambient ionization sources for mass spectrometry.[29–31] Recently, these jets have also been proposed for sampling purposes in depth profiling analysis of metal substrates.[32] In spite of the considerable amount of publications describing new applications of such sources there are few fundamental studies and there is much to be learned of their underlying mechanisms. Spectral imaging has proven very effective in providing information on the spatial distribution of plasma species thus unveiling some of the chemical pathways at the core of these plasma sources under conditions for soft desorption/ionization.[10,11,33]

The plasma gas used for the APPJ here is He and the imaged region of the plasma is exposed to ambient air, thus optical emission from excited plasma gas and air component species is observed. Fig. 8 shows CS spectral images of the atmospheric pressure DBD jet obtained with the 4096 SBHE at 30% sampling, and reconstructed with the GPSR algorithm and wavelet basis. The 4096 SBHE was used to cope with the relatively lower intensity of light. The spectral image obtained at 587.6 nm corresponds to the $2p\ ^3P_J{}^0$–$3p\ ^3D_J$ transition for He I (Fig. 8a). The spectral image obtained at 391.4 nm corresponds to the bandhead from $B^2\Sigma_u{}^+$–$X^2\Sigma_g{}^+$ transition for $N_2{}^+$, 0–0 first negative system (Fig. 8b). The spectral image obtained at 380.4 nm corresponds to the bandhead from $C^3\Pi_u$–$B^3\Pi_g$ transition for N_2, 0–2 second positive system (Fig. 8c). The position of the plasma/sample interface can be clearly observed because there is a reflection of the optical emission. It is evident that the He I emission intensity is brightest inside the fused silica capillary and it decreases from the tip of the capillary to the sample surface. This observation confirms that the He excited species are generated inside the silica capillary, in the vicinity of the active part of the discharge, where electron impact and recombination mechanisms are favored. On the other hand, the $N_2{}^+$ emission intensity is much lower inside the capillary, then reaches a maximum outside and finally decreases at the sample surface. This indicates that $N_2{}^+$ is formed from species generated upstream including Penning ionization[34] with He metastables or charge transfer[11] with He^+ and $He_2{}^+$. In contrast, the N_2 emission intensity keeps increasing until it reaches a maximum at the sample surface. This indicates that N_2 is generated from electron recombination[10] with $N_2{}^+$.

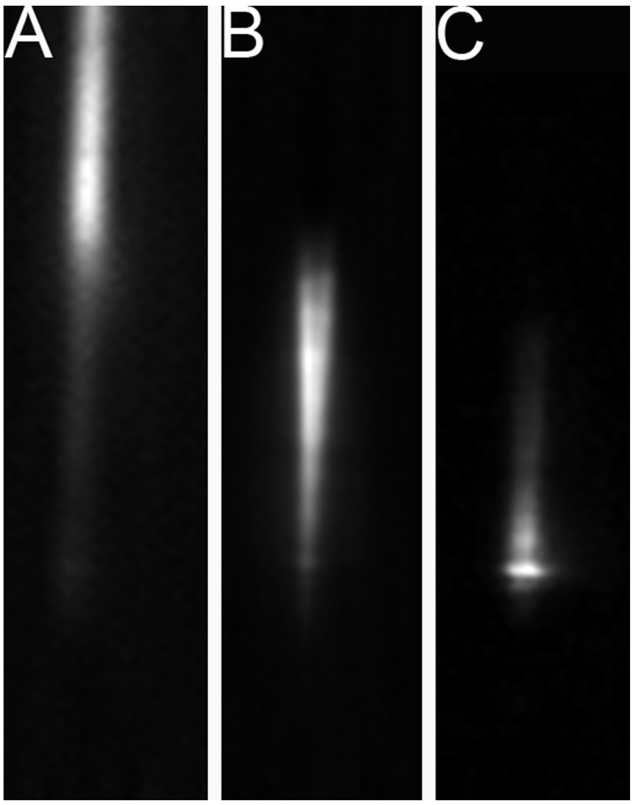

Fig. 8 CS spectral images of the atmospheric pressure DBD jet (4096 SBHE, 30% sampling, GPSR and DWT). (A) He I emission at 587.6 nm. (B) $N_2{}^+$ emission at 391.4 nm. (C) N_2 emission at 380.4 nm. Each image was normalized to the highest intensity within the image. Here, the intensities are not comparable between images.

Another noticeable trend is that the most intense part of the N_2 emission intensity is wider at the sample surface. On the other hand, the $N_2{}^+$ emission is widest just outside the capillary and it becomes much thinner at the sample surface. This is an indication that the $N_2{}^+$ may have an important role in the erosion mechanism of the copper substrate given that reported full width at half maximum of the erosion craters is smaller than the inner diameter of the fused silica.[32] This also points out at the importance of having a full picture of the plasma OES, and not just at the axis, otherwise this information will not be captured.

It is also important to determine the spatially resolved plasma temperatures in order to obtain more information on the plasma energy pathways. Fig. 9 shows the CS spectral images obtained (4096 SBHE, 30% sampling, GPSR, and DWT) that correspond to the bandheads from the $C^3\Pi_u$–$B^3\Pi_g$ transition for N_2 (2–4, Fig. 9a), (1–3, Fig. 9b), and (0–2, Fig. 9c). It is important to note that the experimental settings for acquisition of each image were optimized to maximize the signal differences between the matrix masks in order to get the best image possible. The relative intensities between images were

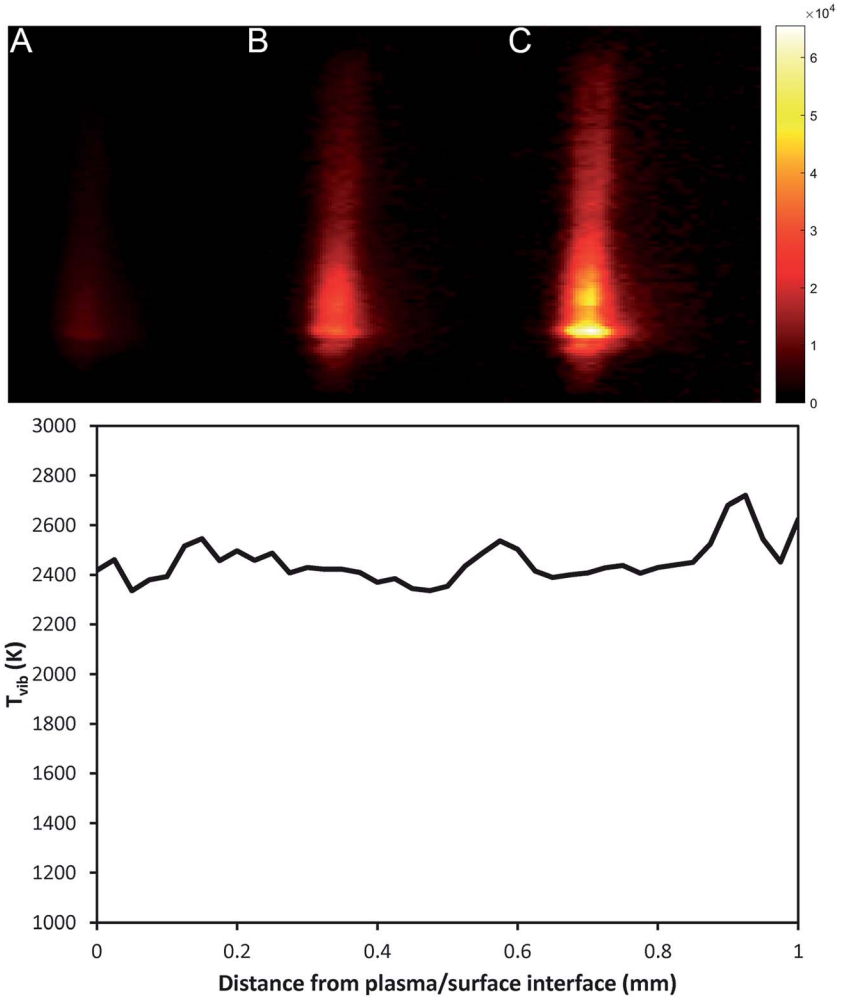

Fig. 9 Top: CS spectral images of the atmospheric pressure DBD jet (4096 SBHE, 30% sampling, GPSR, and DWT) that correspond to the bandheads from the $C^3\Pi_u$–$B^3\Pi_g$ transition for N_2 (2–4, A), (1–3, B), and (0–2, C). Bottom: axial profile of vibrational temperatures calculated from Boltzmann distribution plot.

determined with additional measurements where all of the mirrors of the DMD were turned to the ON position (all mirrors direct light toward the detector) such that the "integrated total intensity" of the plasma was measured at the selected bandhead wavelength. Subsequently, the relative intensity was calculated by normalizing the CS image to its highest intensity, multiplying the normalized CS image by its corresponding "integrated total intensity" measured and dividing the resulting image by the sum of the normalized CS image pixel values.

The images of the transitions measured serve to calculate the vibrational temperature, T_{vib} (Fig. 9d). The T_{vib} is an important parameter because it is calculated from the Boltzmann distribution plot of the vibrational levels. The vibrational levels are separated by high enough energy such that collision of excited N_2 with colder counterparts is not efficient in equilibrating the vibrational distribution. Thus, the T_{vib} is more indicative of the processes that lead to the excitation which is mainly *via* interactions with electrons. As such, T_{vib} can serve to get a clue into the electron energy distribution. This is also part of the reason the observed T_{vib} is much higher than rotational temperatures. The axial T_{vib} profile of the region between the tip of the capillary and the plasma/surface interface shows that it is fairly constant at around 2500 K with a typical relative standard deviation of 10% calculated from the standard deviation of the slope associated with the linear fit of the Boltzmann plots. To the authors' knowledge, this is the first time a CS spectral imaging system is used for plasma diagnostics.

Conclusions

The design and development of a compressed sensing spectral imaging system was accomplished. This is based on spatial encoding of the object through a series of scrambled block Hadamard ensemble matrices. In terms of PSNR, a DWT sparsifying basis and GPSR reconstruction algorithm performed better than other combinations with DCT and TwIST. In addition, it was observed that SBHE matrix size has an effect on the PSNR which was attributed to different kinds of noise. The CS spectral imaging system was implemented for plasma optical emission imaging of an atmospheric pressure plasma jet. An

insight into the plasma can be obtained from these images but it is evident that a systematic study of the effects of the plasma operating parameters is required to best understand the underlying mechanisms. Nevertheless, it is clear that the single-sensor system yields high quality images for an order-of-magnitude lower price *vs.* conventional array detector cameras while circumventing the time restrictions of traditional pixel-by-pixel rastering systems. These advantages will allow spectral imaging to become more accessible and eventually open up further applications.

Acknowledgements

This material is based upon work supported by the National Science Foundation under CHE - 1610849. J. Usala would like to acknowledge funding from the Texas Tech University Center for Active Learning and Undergraduate Engagement, as well as the Texas Tech University Center for the Integration of STEM Education and Research. A. Maag would like to acknowledge funding from Bern University of Applied Sciences International Relations Office. The authors would like to thank S. Shi for help with construction of the APPJ source.

References

1 M. Kroschk, J. Usala, T. Addesso and G. Gamez, *J. Anal. At. Spectrom.*, 2016, **31**, 163–170.
2 G. Gamez, M. Voronov, S. Ray, V. Hoffmann, G. Hieftje and J. Michler, *Spectrochim. Acta, Part B*, 2012, **70**, 1–9.
3 G. C. Y. Chan and G. M. Hieftje, *Anal. Chem.*, 2013, **85**, 50–57.
4 G. C. Y. Chan and G. M. Hieftje, *Anal. Chem.*, 2013, **85**, 58–65.
5 G. Lotito, T. Nelis, P. Guillot and D. Günther, *Spectrochim. Acta, Part B*, 2011, **66**, 619–626.
6 R. Valledor, J. Pisonero, T. Nelis and N. Bordel, *Spectrochim. Acta, Part B*, 2012, **68**, 24–33.
7 G. Chan and G. Hieftje, *Spectrochim. Acta, Part B*, 2005, **60**, 1486–1501.
8 C. Engelhard, G. Chan, G. Gamez, W. Buscher and G. Hieftje, *Spectrochim. Acta, Part B*, 2008, **63**, 619–629.
9 M. J. Van de Sande, P. Van Eck, A. Sola, A. Gamero and J. J. A. M. Van der Mullen, *High Temp. Mater. Processes*, 2003, **7**, 83–91.
10 G. Chan, J. Shelley, A. Jackson, J. Wiley, C. Engelhard, R. Cooks and G. Hieftje, *J. Anal. At. Spectrom.*, 2011, **26**, 1434–1444.
11 G. Chan, J. Shelley, J. Wiley, C. Engelhard, A. Jackson, R. Cooks and G. Hieftje, *Anal. Chem.*, 2011, **83**, 3675–3686.
12 I. Gornushkin, S. Shabanov and U. Panne, *J. Anal. At. Spectrom.*, 2011, **26**, 1457–1465.
13 S. Merk, A. Demidov, D. Shelby, I. Gornushkin, U. Panne, B. Smith and N. Omenetto, *Appl. Spectrosc.*, 2013, **67**, 851–859.
14 M. F. Duarte, M. A. Davenport, D. Takbar, J. N. Laska, T. Sun, K. F. Kelly and R. G. Baraniuk, *IEEE Signal Process. Mag.*, 2008, **25**, 83–91.
15 K. Bryan and T. Leise, *SIAM Rev.*, 2013, **55**, 547–566.
16 D. L. Donoho, *IEEE Trans. Inf. Theory*, 2006, **52**, 1289–1306.
17 D. J. Holland and L. F. Gladden, *Angew. Chem., Int. Ed.*, 2014, **53**, 13330–13340.
18 R. F. Marcia, Z. T. Harmany and R. M. Willett, in *Computational Imaging VII*, ed. C. A. Bouman, E. L. Miller and I. Pollak, 2009, vol. 7246.
19 M. A. Neifeld and J. Ke, *Appl. Opt.*, 2007, **46**, 5293–5303.
20 E. J. Candes, J. Romberg and T. Tao, *IEEE Trans. Inf. Theory*, 2006, **52**, 489–509.
21 E. J. Candes, J. K. Romberg and T. Tao, *Commun. Pure Appl. Math.*, 2006, **59**, 1207–1223.
22 E. J. Candes and M. B. Wakin, *IEEE Signal Process. Mag.*, 2008, **25**, 21–30.
23 G. Gamez, *J. Anal. At. Spectrom.*, 2016, DOI: 10.1039/c6ja00262e.
24 J. A. Tropp and S. J. Wright, *Proc. IEEE*, 2010, **98**, 948–958.
25 L. Gan, T. T. Do and T. D. Tran, *European Signal Processing Conference*, Lausanne, 2008.
26 M. A. T. Figueiredo, R. D. Nowak and S. J. Wright, *IEEE J. Sel. Top. Signal Process.*, 2007, **1**, 586–597.
27 J. M. Bioucas-Dias and M. A. T. Figueiredo, *IEEE Trans. Image Process.*, 2007, **16**, 2992–3004.
28 M. Raginsky, R. M. Willett, Z. T. Harmany and R. F. Marcia, *IEEE Trans. Signal Process.*, 2010, **58**, 3990–4002.
29 A. Albert, J. Shelley and C. Engelhard, *Anal. Bioanal. Chem.*, 2014, **406**, 6111–6127.
30 H. Chen, G. Gamez and R. Zenobi, *J. Am. Soc. Mass Spectrom.*, 2009, **20**, 1947–1963.
31 G. Harris, A. Galhena and F. Fernandez, *Anal. Chem.*, 2011, **83**, 4508–4538.
32 Z. Xing, J. Wang, G. Han, B. Kuermaiti, S. Zhang and X. Zhang, *Anal. Chem.*, 2010, **82**, 5872–5877.
33 J. Shelley, G. Chan and G. Hieftje, *J. Am. Soc. Mass Spectrom.*, 2012, **23**, 407–417.
34 R. B. Cody, J. A. Laramée and H. D. Durst, *Anal. Chem.*, 2005, **77**, 2297–2302.

